Root Cutout Effects on the Aerodynamics of a Low-Aspect-Ratio Revolving Wing

T. Jardin*
Université de Toulouse, 31055 Toulouse, France
and
L. David†
Université de Poitiers, 86962 Chasseneuil, France

DOI: 10.2514/1.J054864

Direct numerical simulations of the flow past a low-aspect-ratio revolving wing are performed. The wing undergoes an impulsively started 180 deg revolution about a vertical axis at angles of attack 15, 30, and 45 deg and chord-based Reynolds number 1000. The root cutout is varied at a fixed wing radius, $R = 4$ chords, and the effects on the flow structure and aerodynamic performance of the wing are evaluated. It is shown that an optimum in aerodynamic efficiency exists at low root cutout. Results suggest that this optimum is due to the competition between low Reynolds number effects at the wing root and root vortex effects. In addition, it is shown that a large root cutout can inhibit leading-edge vortex burst that occurs at high angles of attack. However, despite the associated recovery in pressure forces near the wing tip, this inhibition has no significant impact on aerodynamic performance.

Nomenclature

b	=	wing span, m
C_p	=	sectional pressure coefficient
C_Q	=	torque coefficient
C_s	=	sectional shear coefficient
C_T	=	thrust coefficient
c	=	wing chord, m
F_p	=	sectional pressure force, $\mathrm{N} \cdot \mathrm{m}^{-1}$
F_s	=	sectional shear force, $\mathrm{N} \cdot \mathrm{m}^{-1}$
PL	=	power loading, $\mathrm{N} \cdot \mathrm{W}^{-1}$
Q	=	torque, $\mathrm{N} \cdot \mathrm{m}$
R	=	wing radius, m
r	=	local wing radius, m
r^+	=	nondimensional local wing radius
rco	=	wing root cutout, m
r_g	=	wing radius of gyration, m
T	=	thrust, N
α	=	wing angle of attack, deg
ϕ	=	revolving angle, deg
ω	=	revolving speed, $\mathrm{rad} \cdot \mathrm{s}^{-1}$

I. Introduction

NANODRONES constitute a class of very small (unmanned) autonomous or semi-autonomous aircraft. Their maximum dimension is on the order of the centimeter, which makes them stealthy and well suited to missions of reconnaissance in confined spaces. Such missions further require hovering or low-speed flight capacity. Thus, nanodrones preferably rely on rotating- and flapping-wing concepts, rather than fixed-wing concepts. One of the most elegant examples of these types of aircraft is the flapping-wing RoboBee developed by Wood at the Harvard Microrobotics Lab [1]. The RoboBee has a maximum dimension (wing span) of 3 cm and weighs approximately 60 mg.

Because of their small dimensions, nanodrones operate at very low Reynolds numbers, on the order of $\mathcal{O}(10^2)$–$\mathcal{O}(10^3)$. Yet the aerodynamic performance of an airfoil decreases with decreasing Reynolds number [2]. It is, for example, more difficult to keep the aircraft aloft at these scales because the lift coefficient is reduced with respect to that at larger scales. The underlying question is then how can the reduction in lift coefficient be compensated for at a given wing span (maximum dimension)? One of the solutions consists of increasing the wing chord, which leads to low-aspect-ratio wings.

The aerodynamics of low-aspect-ratio wings is rather complex in that it is driven by three-dimensional effects. For instance, Ringuette et al. [3] and Jardin et al. [4] showed that the tip vortex (TV) that develops on a translating wing at low Reynolds numbers significantly affects the flow in a region that can extend from the wing tip to approximately 1.5 chords away from it. This three-dimensional effect is clearly nonnegligible for low-aspect-ratio wings and becomes predominant for wings with aspect ratio lower than 2, where the flow can be stabilized at high angle of attack [5].

Furthermore, in the specific case of a wing revolving about a vertical axis (span is oriented horizontally), Kruyt et al. [6] showed that the leading-edge vortex (LEV) that develops at high angle of attack is robust (in that it does not eventually shed into the wake) in a region that extends from the axis to approximately four chords away from it. Although initially put into evidence by Ellington et al. [7], and largely held responsible for the good aerodynamic performance of insects [8] and autorotating seeds [9], this phenomenon was not until then clearly associated with a specific region along the span, hence with aspect ratio. Explanations of LEV robustness are still subject to controversy (see for example [10–14]), and we will not go into details here, but it is evident that this robustness arises from three-dimensional effects. Overall, two main classes of three-dimensional effects that derive from revolving motion and that may promote LEV robustness can be identified: 1) spanwise gradient of the local wing speed, and 2) rotational accelerations (centrifugal, Coriolis).

Recently, several studies have focused on analyzing the dynamics of the LEV with regard to previous hypotheses on its robustness (e.g., [12,15,16]). These studies address issues related to LEV behavior by varying a specific scaling parameter (global Reynolds number, Rossby number, and aspect ratio) while keeping others constant. However, because scaling parameters are here defined as global parameters, most studies do not address

Received 5 November 2015; revision received 28 January 2017; accepted for publication 7 February 2017; published online 12 May 2017.

*Research Scientist, Département d'Aérodynamique, Energétique et Propulsion, Institut Supérieur de l'Aéronautique et de l'Espace, 10 Avenue Edouard Belin.

†Professor, Département Fluides, Thermique et Combustion, Institut Pprime, 11 Boulevard Marie et Pierre Curie.

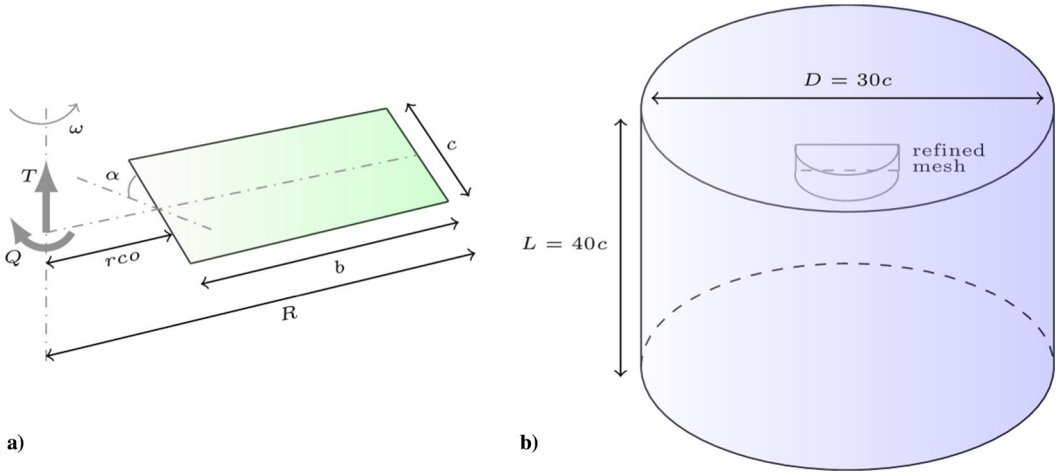

Fig. 1 Geometry of a) revolving wing, and b) computational domain.

constant distribution in local scaling parameters (along the span). It is believed that local scaling parameters are the key element in local LEV behavior and are crucial for the study of low-aspect-ratio wings, where the LEV can transition from a stable to an unstable state along the span. This approach has recently been addressed by Garmann and Visbal [12], who analyzed the role of aspect ratio at fixed root cutout and fixed root Reynolds number, matching both distributions in local Reynolds number and local Rossby number, from the wing root toward the wing tip, of all configurations. Yet another case should be considered to complete the picture, that where both distributions in local Reynolds number and local Rossby number, from the wing tip toward the wing root, are matched. This case can be analyzed by investigating root cutout effects. The latter can be viewed as an aspect ratio effect mediated by variations in root vortex (RV) strength. Although intrinsically present in the previously cited studies, root cutout effects were only briefly addressed by Schlueter et al. [17] using lift measurements performed on a revolving flat plate at angle of attack $\alpha = 45$ deg and Reynolds number (based on the wing chord and the wing speed at 75% span) of 10,000. In particular, there is no evidence of how the dynamics of the LEV is affected, how the loads distribution along the wing span is altered, or even if increasing the root cutout has a beneficial impact on the aerodynamic performance of a revolving wing.

This paper proposes to answer these questions using direct numerical simulations (DNS) of the flow past a revolving flat plate at Reynolds number (based on the wing chord and the wing speed at the tip) of 1000. The wing aspect ratio is varied from 4 to 1 by increasing the root cutout and keeping the radius constant ($R = 4$ chords) for angles of attack $\alpha = 15, 30$, and 45 deg. Cases addressed in this study are highly relevant to the development of nanodrones where the wing radius, which is usually the maximum dimension of the vehicle, is a primary constraint. In addition, they stand as intermediary cases between common cases addressed in the literature (i.e., zero root cutout rotating wing cases where root vortex effects are minimized and translating wing cases where root vortex effects are maximized).

II. Numerical Setup

We consider a rectangular wing, with a 4% thick flat plate profile, undergoing a $\phi = 180$ deg impulsively started revolution about a vertical axis (Fig. 1a). The wing tip is located $R = 4$ chords away from the axis. The root cutout (or location of the wing root from the axis) is set to rco = 0, 1, 2, and 3 chords, leading to aspect ratio $\mathrm{AR} = b/c = 4, 3, 2$, and 1 and Rossby numbers $\mathrm{Ro} = r_g/c = 2.3$, 2.6, 3, and 3.5, respectively. Recall that b, c, and r_g are the span, chord, and radius of gyration of the wing. Also recall that the radius of gyration is defined as

$$r_g = \sqrt{\frac{1}{A}\int_{\text{root}}^{\text{tip}} r^2 c \, \mathrm{d}r}$$

where A and r are the area and local radius of the plate, respectively. The angle of attack is set to $\alpha = 15, 30$, and 45 deg. The Reynolds number based on the wing chord c and the wing speed at the tip ωR is set to 1000. Reynolds number and Ro are global quantities defined with respect to the wing radius R and radius of gyration r_g respectively. Their local counterparts $Re(r)$ and $\mathrm{Ro}(r)$ can be defined using the local radius r.

The wing is embedded in a cylindrical computational domain of diameter $30c$ and length $40c$ (Fig. 1b). The flow in the domain is computed by directly resolving the Navier–Stokes equations (DNS), in their incompressible form, following a finite volume approach. The size of the cells in the vicinity of the wing (refined mesh region on Fig. 1b) is set to $\Delta s = 0.02c$ in all three spatial directions. The total number of cells is approximately 10 million. The time step Δt used for time marching of the equations corresponds to a $\Delta\phi = 1$ deg revolution. Second-order schemes are used for both spatial and temporal discretizations.

Time step and cell size are chosen such that convergence in time and space is achieved while minimizing the computational time. Convergence is defined as a variation in instantaneous and mean aerodynamic loads (both wing thrust T and torque Q), with respect to a reference solution, lower than 2 and 0.5%, respectively. Table 1 provides an example of the variations in thrust obtained for various time step Δt (expressed in revolution angle $\Delta\phi$) and cell size Δs (characteristic size in the refined mesh region; the total number of cells is indicated in brackets) for the baseline case $\alpha = 45$ deg and rco = 0. In addition, Fig. 2 depicts the time histories of the thrust C_T and torque C_Q coefficients for various cell size. C_T and C_Q are obtained by nondimensionalizing T and Q by the wing surface $c \times b$ and the wing speed at the radius of gyration $\omega \times r_g$. As found in

Table 1 Variations in instantaneous/mean thrust with time step and cell size

$\Delta\phi/\Delta s$, deg	$0.01c$ (72 million)	$0.015c$ (22 million)	$0.02c$ (10 million)	$0.025c$ (5 million)
0.25	Reference	0.92%/0.04%	0.92%/0.10%	1.87%/0.52%
0.5	— —	— —	1.05%/0.16%	— —
1	— —	— —	1.07%/0.10%	— —

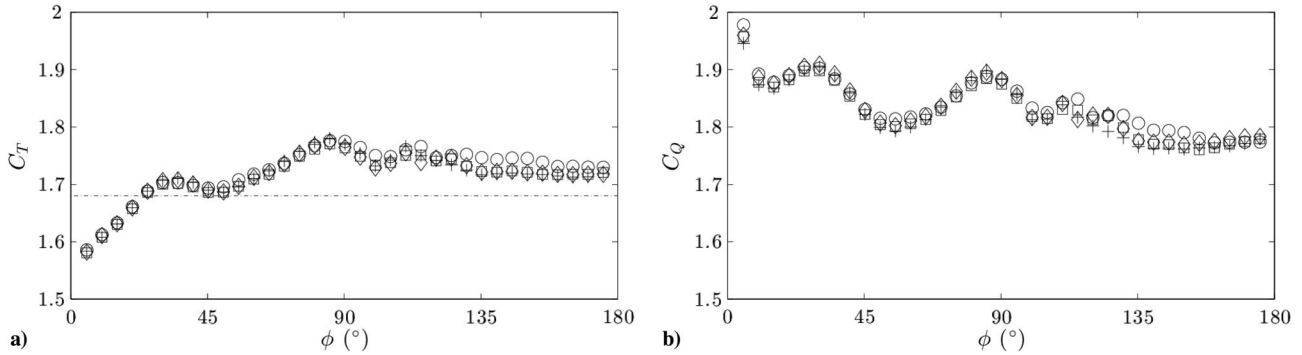

Fig. 2 Time histories of thrust (C_T) and torque (C_Q) coefficients obtained for various cell size: $\Delta s = 0.01c$ (+), $0.015c$ (⋄), $0.02c$ (□), and $0.025c$ (○).

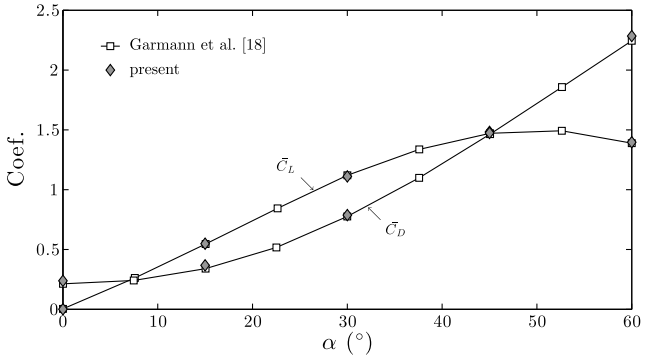

Fig. 3 Comparison between mean lift and drag coefficients obtained using the present approach with those obtained by [18] for a wing with aspect ratio 1.

previous works, aerodynamic loads roughly reach a steady-state value for angle of revolution typically above 120 deg (and before a full revolution is reached) [16]. For the sake of comparison, the steady-state value obtained experimentally by Carr et al. [16] for a similar case at a Reynolds number (based on the wing chord and the wing speed at the tip) of 5780 is depicted by the dashed line. The latter is approximately 2% away from that obtained using the present numerical approach. Additional tests were also performed to ensure that the results are also converged with respect to the size of the computational domain and that of the refined mesh region. Increasing the size of the computational domain up to $50c \times 60c$ and doubling the size of the refined mesh region, for $\Delta\phi = 1$ deg and $\Delta s = 0.02c$, results in negligible changes in both instantaneous and mean thrust (i.e., below 0.03%) for a significant increase in total number of cells, on the order of 18 million.

Furthermore, the results obtained using the present numerical approach (with $\Delta s = 0.02c$, $\Delta t = 2\pi/360$) are compared with those obtained in [18] for a revolving wing with aspect ratio AR $= 1$ and root cutout rco $= 0.52c$ (i.e., radius $R = 1.02c$). The Reynolds number based on the wing speed at midspan is 500, which is close to that considered in the present paper. Figure 3 shows this comparison in terms of mean lift $\bar{C}_L$ (or mean thrust $\bar{C}_T$) and drag $\bar{C}_D$ coefficients over angles of attack ranging from 0 to 60 deg, which encompass angles of attack tested here. Note that mean values are computed by integrating instantaneous values over revolution angles $\phi \in [45 \text{ deg} - 315 \text{ deg}]$. It can be seen that relatively good agreement is achieved between both approaches.

Finally, it should also be mentioned that the finite volume method employed here has already proven its ability to accurately predict the occurrence of flow instabilities at low Reynolds numbers [19].

III. Results

A. Flow Structure

Figure 4 shows a snapshot sequence of λ_2 isosurfaces obtained for the baseline case $\alpha = 45$ deg and rco $= 0$. Rapidly after the impulsive start ($\phi = 30$ deg), the flow is characterized by the development of a starting vortex (SV), a leading-edge vortex (LEV), a tip vortex (TV), and a root vortex (RV). These structures connect into a coherent vortex loop, where coherency is here defined in the large-scale sense (i.e., a structure composed of multiple small-scale structures is said to be noncoherent). Afterward, the LEV in the outboard region of the wing lifts off the wing surface ($\phi = 60$ deg) and eventually bursts into a noncoherent structure ($\phi = 90$ deg). The initial bursting phase exhibits a clear upward eruption of the noncoherent structure in the wake of the wing tip ($\phi = 120$ deg). Two distinct regions can then be identified: 1) the inboard region characterized by the development of a coherent and robust conical

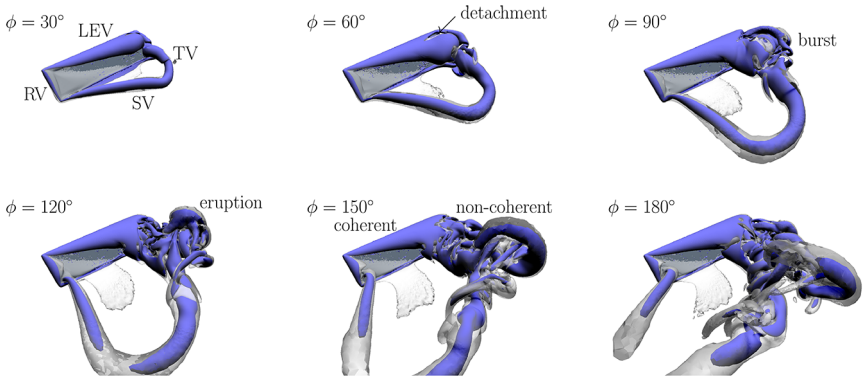

Fig. 4 Snapshot sequence of λ_2 isosurfaces obtained for the baseline case $\alpha = 45$ deg and rco $= 0$. Nondimensional λ_2 values 1 (opaque) and 0.1 (transparent).

LEV, and 2) the outboard region characterized by the merging of the LEV and TV and their bursting into a noncoherent structure that is advected into the wake.

The scenario pertaining to LEV burst is usually described as a sudden expansion of the LEV that is correlated with deceleration of its axial core flow, subsequently leading to an overall loss of coherency. The whole process from impulsive start to vortex burst is relatively well documented in the literature (e.g., [12,15,16,20–25]) and will therefore not be further detailed here. Rather, we ask to what extent does the root cutout affect this dynamics? Figure 5 shows snapshots of λ_2 isosurfaces obtained at $\phi = 120$ deg for rco $= 0$, $1c$, $2c$, and $3c$ and $\alpha = 15$, 30, and 45 deg. Similar snapshots for $\phi = 180$ deg are provided in the Appendix. Overall, the flow exhibits a roughly similar structure for all cases, in the sense that it consists of the prominent ingredients previously put into evidence (i.e., the SV, LEV, TV, and RV). However, the vortex dynamics, and in particular the bursting phase, is significantly affected by both rco and α.

First, it appears that the extent of the outboard bursting region decreases with decreasing α and even vanishes at $\alpha = 15$ deg (e.g., Figs. 5a–5c). At $\alpha = 15$ deg, the flow retains coherency throughout the whole motion, regardless of rco (Figs. 5a, 5d, 5g, and 5j). At $\alpha = 30$ deg, vortex burst is more confined toward the wing tip than at $\alpha = 45$ deg (Figs. 5b and 5c) but is found to occur at similar instants. In particular, vortex burst is found to extend over a portion of the wing on the order of $r_b = 1.3$ and $r_b = 1.7$ chords in the $\alpha = 30$ deg and $\alpha = 45$ deg cases, respectively (see λ_2 isosurfaces expansion on Figs. 5b, 5c, 5e, and 5f), and occurs around $\phi = 90$ deg for both angles of attack.

Second, as expected, an increase in RV strength is observed with increasing rco (e.g., Figs. 5a, 5d, 5g, and 5j). Despite this increase, the root cutout effects do not seem to have a major impact on LEV dynamics and vortex burst for rco $= 0$, $1c$, and $2c$ (Figs. 5b, 5c, 5e, 5f, 5h, and 5i). However, root cutout effects completely inhibit vortex burst for rco $= 3c$ (Figs. 5k and 5l). In a rather similar way to what can be observed on a translating wing [4], the RV and TV dominate the flow that subsequently tends toward a coherent and nearly steady state (Figs. 5j–5l). We also note in passing that, as rco increases and the RV gains strength and gets closer to the TV, mutual induction between the counter-rotating RV and TV seems to be responsible for the kink observed in the root vortex trail (e.g., Figs. 5h and 5i). In some cases, this may lead to the formation of vortex loops farther downstream (Figs. 5k and 5l), which has also been observed on low-aspect-ratio translating wings (e.g., [26]).

B. Loads Distribution

How do these interactions affect loads distribution on the wing? Figures 6a, 6b compare the nondimensional pressure C_p and shear C_s force distributions, as a function of the nondimensional radial position r^+, obtained at the end of the motion $\phi = 180$ deg for rco $= 0, 1c, 2c$, and $3c$ and $\alpha = 15$ deg. C_p and C_s are obtained by nondimensionalizing F_p and F_s by $(1/2)\rho(\omega R)^2 c$, where F_p and F_s are the sectional pressure and shear forces acting perpendicularly to the wing span. That is, combining and integrating F_p and F_s (and $r \times F_p$ and $r \times F_s$) along the wing span gives the wing thrust (and rotational torque). Note that F_p and F_s are computed over $50 \times$ AR overlapping sections of width $R/20$. r^+ is obtained by nondimensionalizing the radial position r by the wing chord c. We focus on the quasi-steady-state regime ($\phi > 120$ deg) for two main reasons. First, results are less dependent on the wing acceleration profile (which is here infinite) than during initial transients and are, in that sense, more universal. Second, they are believed to be representative of the flow after multiple rotations, albeit with a different effective angle of attack (downwash due to multiple rotations tends to reduce the effective angle of attack).

The sectional pressure coefficient C_p (Fig. 6a) increases with increasing spanwise position r^+ following a parabolic trend, according to the increase of the local wing speed ωr, until the influence of the TV is felt. Toward the wing tip, the downwash

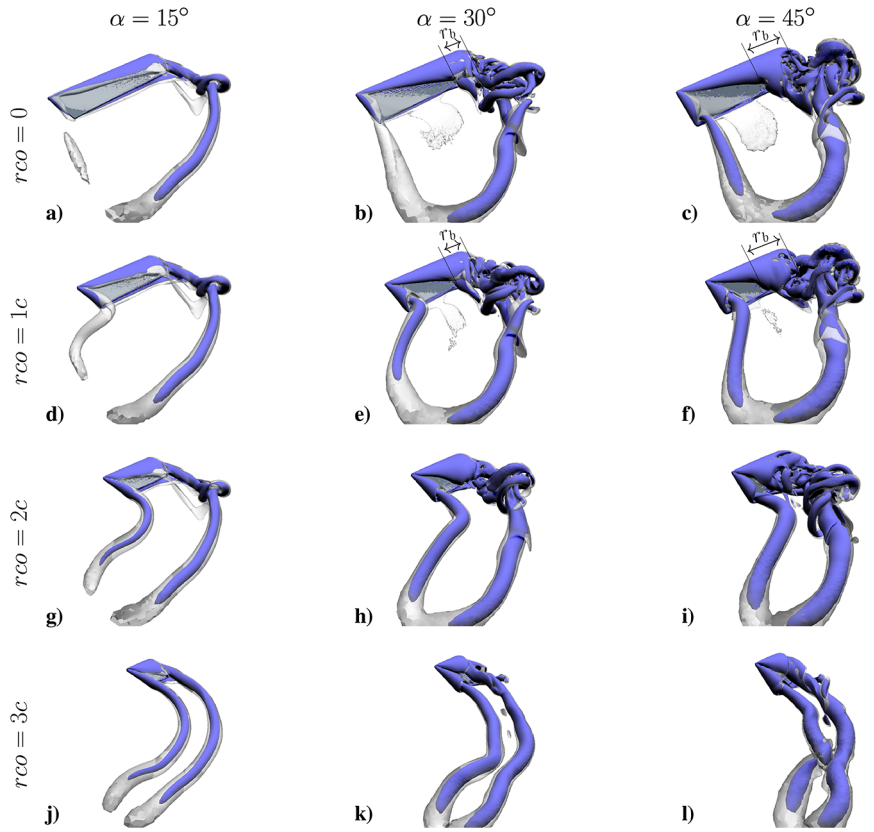

Fig. 5 Snapshots of λ_2 isosurfaces obtained for all cases at $\alpha = 15$ deg. Nondimensional λ_2 values 1 (opaque) and 0.1 (transparent).

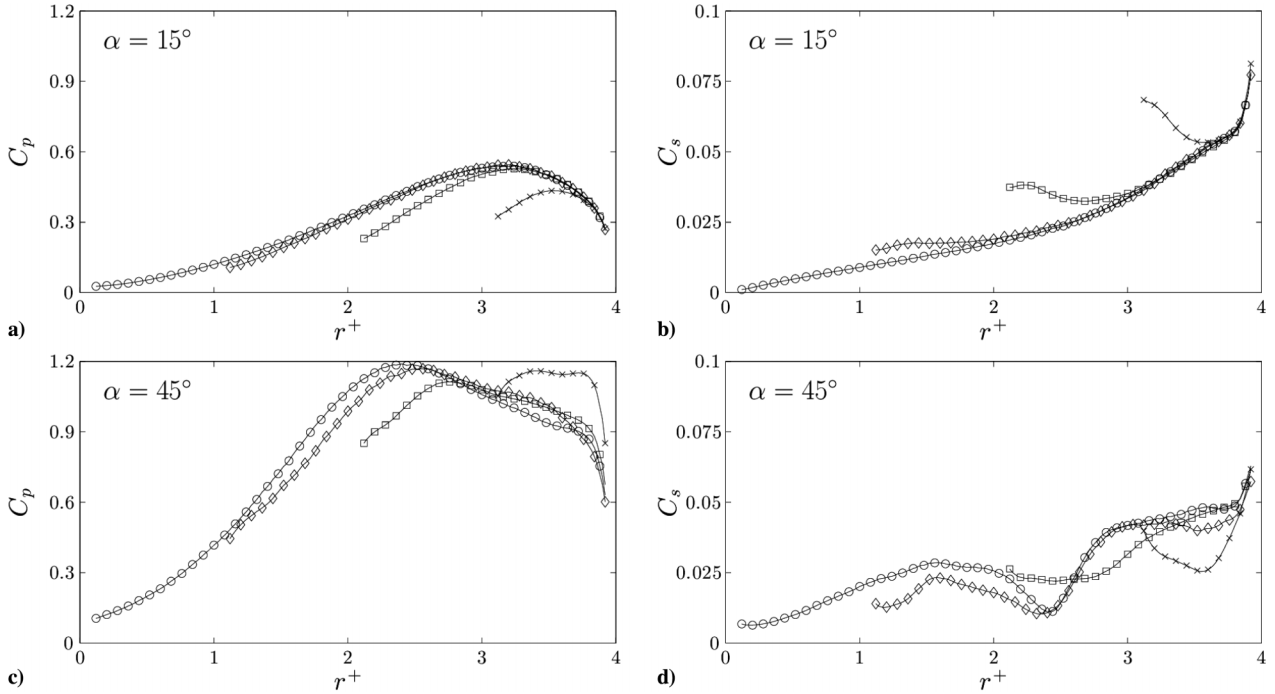

Fig. 6 C_p (Figs. 6a, 6c) and C_s (Figs. 6b, 6d) as a function of r^+ for rco = 0 (∘), 1c (⋄), 2c (□), and 3c (×), with $\alpha = 15$ deg (Figs. 6a, 6b) and $\alpha = 45$ deg (Figs. 6c, 6d).

induced by the TV mitigates the effective local angle of attack, which counteracts the effect of an increasing local wing speed. As a result, a local maximum of C_p is observed at approximately 0.8–0.9 chords from the wing tip for cases where rco = 0, 1c, and 2c. In the inboard region, C_p decreases with increasing rco for a given radial position r^+. This trend highlights the influence of the RV induced downwash whose strength increases with increasing rco. The interaction between the RV and the TV is not significant for cases where rco = 0 and 1c and is still very limited when rco = 2c, as indicated by roughly similar position and amplitude of the maximum C_p. This is no more true in the case where rco = 3c, for which downwash effects from both RV and TV combine, thereby significantly reducing the maximum value of C_p and pushing it toward the wing tip.

In a similar way, according to the increase of the local wing speed ωr, the sectional shear coefficient C_s (Fig. 6b) increases with increasing spanwise position r^+. However, the RV and TV have an opposite impact on C_s from that observed on C_p, in that they do not counteract but combine with the effect of increasing local wing speed. In the outboard region, C_s strongly increases due to TV induced shear. In the inboard region, C_s increases with increasing rco (i.e., increasing RV strength and associated shear) for a given radial position r^+, leading to local C_s minima for sufficiently strong RVs (rco = 2c and 3c). TV and RV footprints are therefore clearly visible on both C_p and C_s distributions.

Figures 6c, 6d compare C_p and C_s distributions for $\alpha = 45$ deg. Here again, the sectional pressure coefficient C_p (Fig. 6c) obtained for rco = 3c stands out from that obtained for rco = 0, 1c, and 2c. However, these changes in C_p trend with rco have a fundamentally different origin from that highlighted when $\alpha = 15$ deg. As previously mentioned, when $\alpha = 45$ deg, cases where rco = 0, 1c, and 2c experience vortex burst. This phenomenon balances the increase in C_p due to increasing local wing speed even before downwash effects from the TV can be felt. As a result, the maximum local value of C_p is pushed toward the wing root. The displacement of local C_p maxima with vortex burst was also recently put into evidence by Garmann and Visbal [12]. Conversely, no such mechanism can be observed for rco = 3c. Rather, the trend in C_p distribution resembles that observed when $\alpha = 15$ deg. It is therefore possible to correlate the absence of premature C_p drop along the span with the absence of vortex burst. As such, although at $\alpha = 15$ deg, the rco = 3c case exhibits a decrease in C_p (at a given r^+ and with respect to rco = 0, 1c, and 2c cases) due to RV and TV downwash, the rco = 3c case at $\alpha = 45$ deg exhibits an increase in C_p. In other words, root cutout effects become locally beneficial because of their influence on coherency recovery.

The distribution in sectional shear coefficient C_s is more complex (Fig. 6d). For the rco = 0 and 1c cases, an overall increase in C_s with r^+ can be observed, yet with a local minimum that seems to coincide with the frontier between the inboard coherent and outboard noncoherent regions on Figs. 5c and 5f. In the rco = 2c case, there is no clear evidence of such a minimum because the frontier nearly coincides with the wing root. Through which specific mechanisms the transition between coherent and noncoherent regions reduces C_s remains unclear at this point. What is more, the strong interaction between the RV and TV and the absence of vortex burst in the rco = 3c case also seem correlated with a local reduction in C_s. Finally, it is noteworthy to mention that, contrary to $\alpha = 15$ deg cases, there is no clear evidence of the RV increasing local C_s at a given r^+ as rco increases.

C. Aerodynamic Performance

C_p and C_s distributions help link the flow physics to the aerodynamic performance displayed on Fig. 7. From a practical perspective, we first look at the dimensional power loading $PL = T/\omega Q$ versus thrust T map in Fig. 7a. Reported values are instantaneous values obtained at the end of the revolving motion ($\phi = 180$ deg) where aerodynamic loads reach a quasi-steady value. It can be seen that a single wing ($c = 0.01$ m and $\omega \approx 40$ rad/s) can produce a thrust on the order of $\mathcal{O}(10^1)$ mg for an efficiency on the order of $\mathcal{O}(10^2)$ mg/mW. For comparative purposes, two wings at $\alpha = 45$ deg and rco = 1c approximately produce a 60 mg thrust, which can be correlated with the weight of the RoboBee [1], at similar scales.

Obviously, T decreases with increasing rco, according to the reduction in wing surface. In the $\alpha = 15$ deg cases, the torque Q mainly arises from shear forces. Although shear forces also tend to decrease with increasing rco because of a reduction in wing surface, they tend to locally increase because of RV effects. Therefore, the effect of the RV on shear forces and torque balances the effect of wing

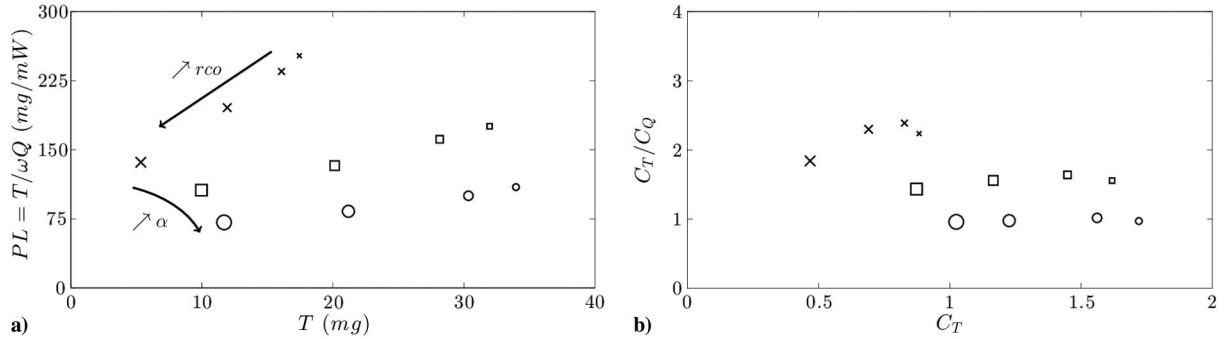

Fig. 7 a) Dimensional, and b) nondimensional PL vs T map obtained for rco $= 0, 1c, 2c$, and $3c$ (symbol size increases with rco); $\alpha = 15$ deg (×), 30 deg (□), and 45 deg (◦).

surface. As a result, PL also decreases with increasing rco. In the $\alpha = 45$ deg cases, the torque mainly arises from pressure forces, which equally contribute to thrust. Therefore, the decrease in thrust with increasing rco is accompanied by a decrease in torque, hence only weak changes in PL.

T also increases with increasing α, together with the increase in LEV strength and associated pressure forces. In addition, because pressure forces are an order of magnitude higher than shear forces, and because pressure forces have a decreasing contribution to T and an increasing contribution to Q with increasing α, PL decreases with increasing α.

However, revealing which of these cases is the more aerodynamically efficient is not straightforward using dimensional quantities. In particular, different revolving wings should not be compared at a given revolving speed ω, but at a given thrust T, which is computationally much more expensive. This issue can partly be tackled by analyzing the nondimensional power loading C_T/C_Q versus thrust C_T map, where C_T and C_Q are obtained by nondimensionalizing T and Q (or ωQ) by the wing surface $c \times b$ and the wing speed at the radius of gyration $\omega \times r_g$. Figure 7b shows that, although maximum C_T is obtained at minimum rco for all α, rco $= 1c$ cases lead to maximum C_T/C_Q values. Note that a similar result is obtained if the mean wing speed along the wing span rather than the wing speed at the radius of gyration is used for nondimensionalization.

As such, in terms of aerodynamic performance, there is no significant interest in increasing rco to inhibit vortex burst at high α. Rather, the impact of the RV in its own is detrimental to aerodynamic efficiency. On the other hand, introducing a small root cutout seems beneficial, particularly at low α values. This suggests that the very inboard part of the wing is detrimental to aerodynamic efficiency, which can be correlated with the decrease in local Reynolds number toward the revolving axis. In other words, present results suggest that maxima in aerodynamic efficiency arise from the relative importance of low Reynolds number effects and root vortex effects.

IV. Discussion

Flows past low-aspect-ratio rotating wings involve complex three-dimensional effects that are known to significantly alter the behavior of the LEV, with respect to that observed on two-dimensional translating wings. A ubiquitous feature observed in nature, and which arises from three-dimensional effects, concerns LEV robustness (i.e., the ability of the LEV to remain attached to the wing for very long time travels). Local LEV robustness along the span of a rotating wing is believed to be driven by local scaling parameters. In this regard, the approach addressed in the previous section allows to keep constant the distributions in both local Reynolds and Rossby numbers, from the wing tip toward the wing root. This approach is rather similar to that addressed by Garmann and Visbal [12] where distributions in both local Reynolds and Rossby numbers are kept constant from the wing root toward the wing tip. Together with the study by Garmann and Visbal [12], results shown in the previous section are complementary to previous works where global scaling parameters (rather than local) are chosen as fixed parameters and constitute a missing step in our understanding of low-aspect-ratio rotating-wing aerodynamics.

In this section, we further discuss the role of local scaling parameters on LEV behavior. The latter can be revealed by comparing cases addressed in the previous section with cases at similar tip Reynolds number ($Re = 1000$) and with similar aspect ratio but with zero root cutout (Fig. 8). The striking feature here is that, contrary to cases where rco $\neq 0$ (Figs. 8a–8c), the extent of the region where vortex burst occurs is significantly reduced as the aspect ratio is reduced for zero root cutout cases (Figs. 8g–8i). In particular, the rco $= 0$ and AR $= 2$ (Fig. 8h) case does not show clear evidence of vortex burst, which appears to be confined in the very tip region, over a portion of the wing on the order of $r_b = 0.7$ chord (as compared to r_b on the order of 1.2 for AR $= 3$). This is fundamentally different from what can be observed in the rco $= 2$ and AR $= 2$ case (Fig. 8b), where vortex burst occurs along most of the wing span. Such a difference seems to indicate that local Rossby number drives vortex burst. It should be emphasized that the local convective time is intrinsically related to the local Rossby number, which obviously suggests differences between cases with different distribution in local Rossby number at a given revolution angle ϕ. However, comparing flows at similar local convective times shows similar differences in the occurrence of vortex burst (Fig. 9). Moreover, the prominent role of the local Rossby number can further be highlighted by comparing nonzero root cutout cases at tip Reynolds number $Re = 1000$ (Figs. 8a–8c) with nonzero root cutout cases at $Re = 1000/\text{rco}$ (Figs. 8d–8f) as well as zero root cutout cases at $Re = 1000$ (Figs. 8g–8i) with zero root cutout cases at $Re = 250 \times \text{AR}$ (Figs. 8j–8l). Note that setting $Re = 1000/\text{rco}$ ensures a similar root Reynolds number, hence similar root vortex strength, for nonzero root cutout cases shown in Figs. 8d–8f. Besides, setting $Re = 250 \times \text{AR}$ ensures similar distribution in local $Re(r)$, from root to tip, for cases shown in Figs. 8j–8l. Corresponding distributions of local $Re(r)$ are displayed in the Appendix. Overall, because cases with similar rco and AR (i.e., similar distribution in local $\text{Ro}(r)$) but different Reynolds number show very similar flow behavior, yet with a decrease in vortex strength as Re decreases, the comparison (between Figs. 8b, 8e, Figs. 8c, 8f, Figs. 8g, 8j, Figs. 8h, 8k, and Figs. 8i, 8l) indicates that the local Reynolds number is not the mediating factor in the occurrence of vortex burst (at least within the range of Reynolds number tested), thereby further supporting the idea that the local Rossby number is the key element. This is consistent with previous works on LEV robustness over rotating wings [10,14].

Root cutout effects can be viewed as an aspect ratio effect mediated by the presence of a root vortex and asymmetry between root and tip vortex strengths. The preceding comparisons show that aspect ratio effects depend on whether or not vortex burst occurs and are therefore dependent on local Rossby number distribution. Besides, the Rossby number reflects the asymmetry in root and tip vortex strengths. As such, cases addressed in this study represent intermediary cases

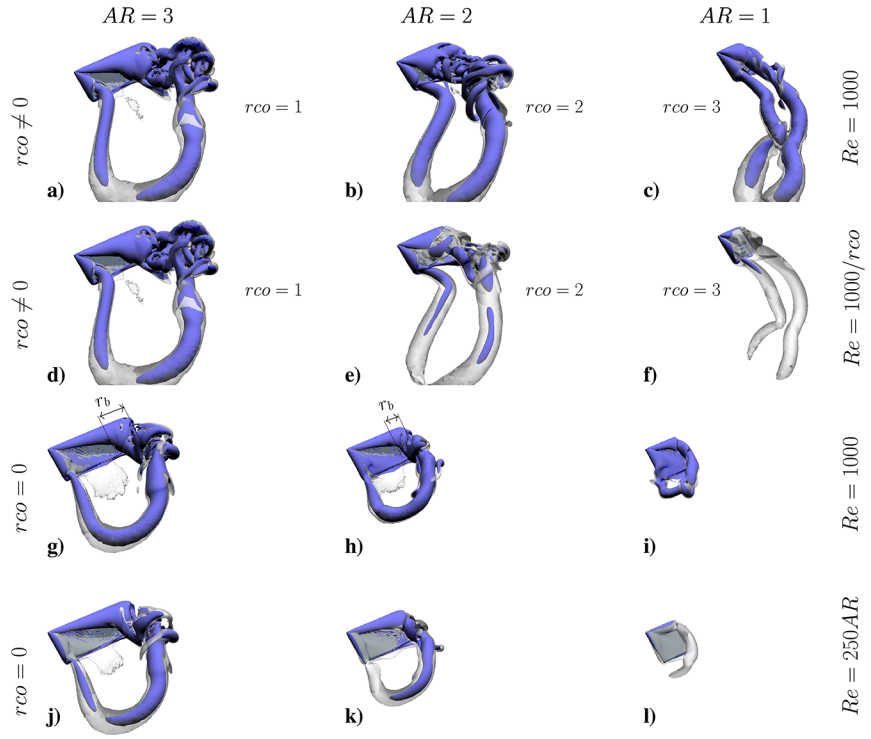

Fig. 8 Snapshots of λ_2 isosurfaces obtained for rco = 0 cases at $\phi = 120$ deg. Comparison with rco ≠ 0 cases. Dimensional λ_2 values are similar to those used in previous figures.

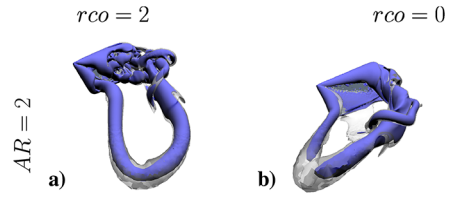

Fig. 9 Snapshots of λ_2 isosurfaces obtained for rco = 2 and rco = 0 cases at $\phi = 90$ deg and $\phi = 180$ deg respectively. AR = 2 and Re = 1000 in both cases.

between 1) zero root cutout rotating wing cases where root vortex effects are minimized, asymmetry is maximized, and the flow is mostly stable; and 2) translating wing cases where root vortex effects are maximized, asymmetry is minimized, and the flow is mostly unstable. A particular drawback though in analyzing such cases is that, although root vortex effects clearly appear for larger aspect ratios, they can hardly be distinguished from aspect ratio effects for lower aspect ratios.

V. Conclusions

DNSs of the flow past a low-aspect-ratio revolving wing at angles of attack $\alpha = 15$, 30, and 45 deg were performed. The wing motion consists of a $\alpha = 180$ deg revolution about a vertical axis (wing span is directed along a horizontal axis) at a wing tip speed and chord-based Reynolds number of 1000. The root cutout has been varied at fixed wing radius $R = 4$ chords, and the effects on the global flow structure and aerodynamic loads have been evaluated.

At low α, the flow structure is fully coherent. On one hand, the root vortex (RV) resulting from root cutout tends to increase local shear forces and decrease local pressure forces due to induced downwash and reduction in local effective angle of attack near the wing root. The RV is therefore detrimental to aerodynamic performance. On the other hand, reduction in local Reynolds number near the wing root, due to the reduction in local wing speed, makes the very inboard part of the wing inefficient. As such, increasing root cutout tends to both increase aerodynamic performance by avoiding low Reynolds number effects near the root and decrease aerodynamic performance by generating a RV. Results suggest that the competition between RV effects and low Reynolds number effects leads to an optimum root cutout in terms of aerodynamic efficiency.

At high α, the flow structure is locally noncoherent near the wing tip due to leading-edge vortex (LEV) burst. The latter is associated with a drop in local pressure forces toward the wing tip. Results show that root cutout effects can inhibit LEV burst at sufficiently large root cutout, hence recovering the associated drop in local pressure forces. However, at large root cutout, the flow is dominated by three-dimensional effects arising from root and tip vortices. It appears that the recovery in local pressure forces due to the inhibition of LEV burst does not compensate for the detrimental effect of root and tip vortex downwash. Therefore, there is no significant interest in inhibiting LEV burst through root cutout effects in terms of aerodynamics performance. Yet for the same reasons as described previously (competition between RV effects and low Reynolds number effects), an optimum root cutout can be found at high α, similar to that observed at low α.

From a practical perspective, it is further interesting to note that root cutout also tends to reduce the wing weight. Although weak for nanodrones, this mass effect combines with aerodynamic effects such that low root cutout is found to be a relevant approach for the enhancement of nanodrone endurance.

Appendix: Flow Structure and Distribution in Local Reynolds and Rossby Numbers

Additional snapshots of λ_2 isosurfaces shown in Figs. 5 and 8 are here provided for $\phi = 180$ deg, in Figs. A1 and A2, respectively. These snapshots allow direct comparison with data provided in Figs. 6 and 7 and show that flowfields at $\phi = 120$ deg (Figs. 5 and 8) and $\phi = 180$ deg (Figs. A1 and A2) are very similar, which illustrates quasi-steadiness of the solution for $\phi > 120$ deg.

In addition, for cases shown in Figs. 8 and A2, distributions in local Reynolds and Rossby numbers are provided in Fig. A3.

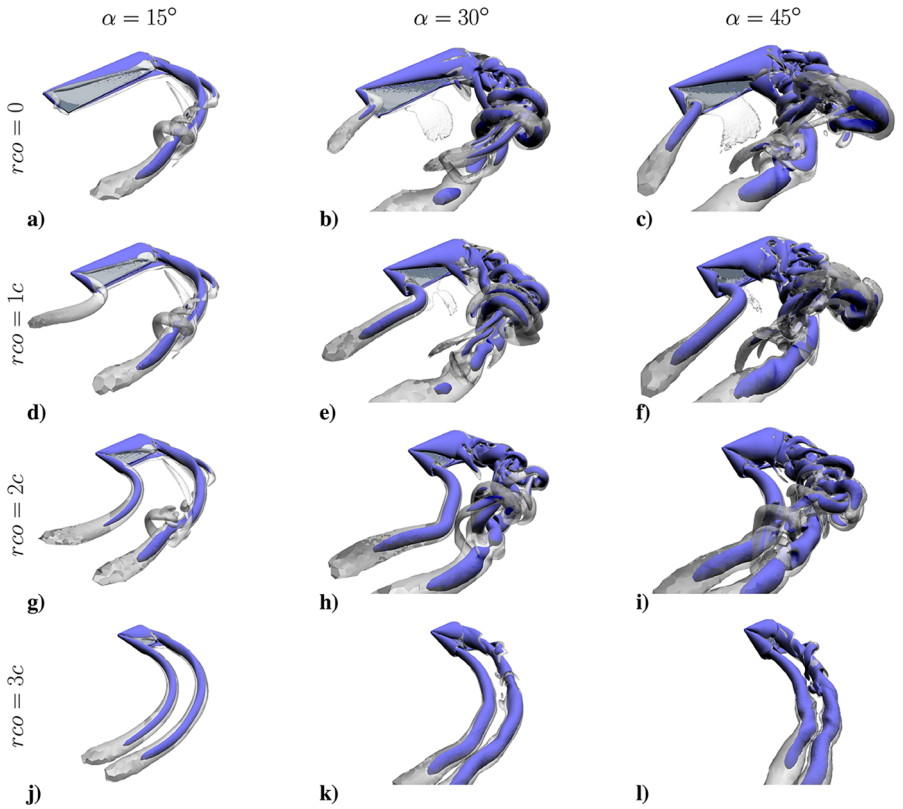

Fig. A1 Snapshots of λ_2 isosurfaces obtained for all cases at $\phi = 180$ deg. Nondimensional λ_2 values 1 (opaque) and 0.1 (transparent).

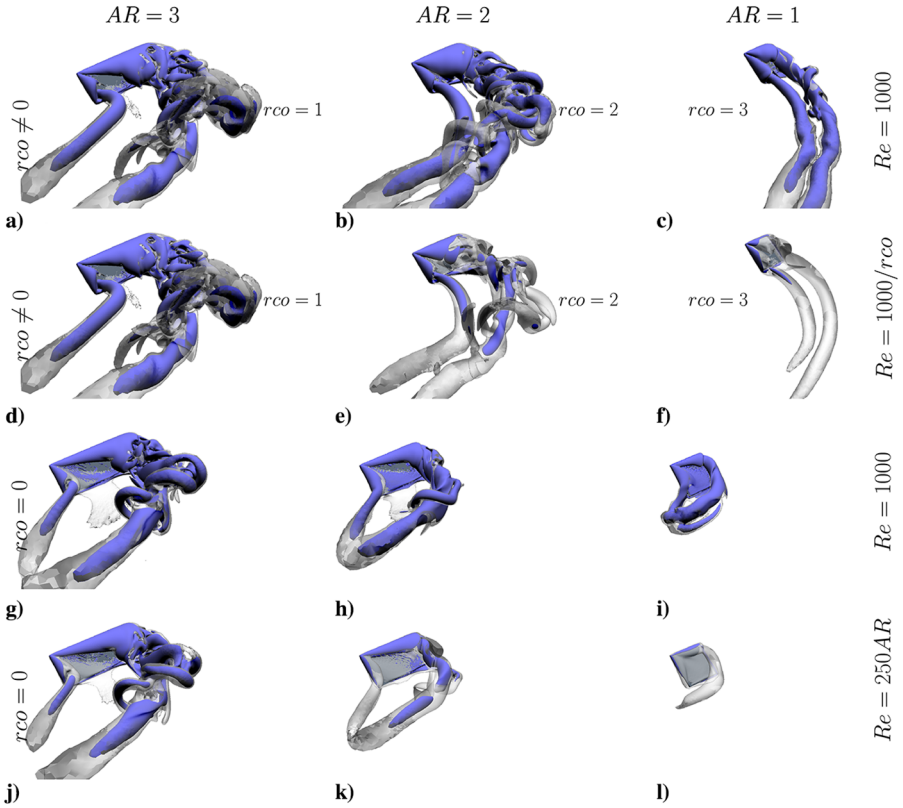

Fig. A2 Snapshots of λ_2 isosurfaces obtained for rco $= 0$ cases at $\phi = 180$ deg. Comparison with rco $\neq 0$ cases. Dimensional λ_2 values are similar to those used in previous figures.

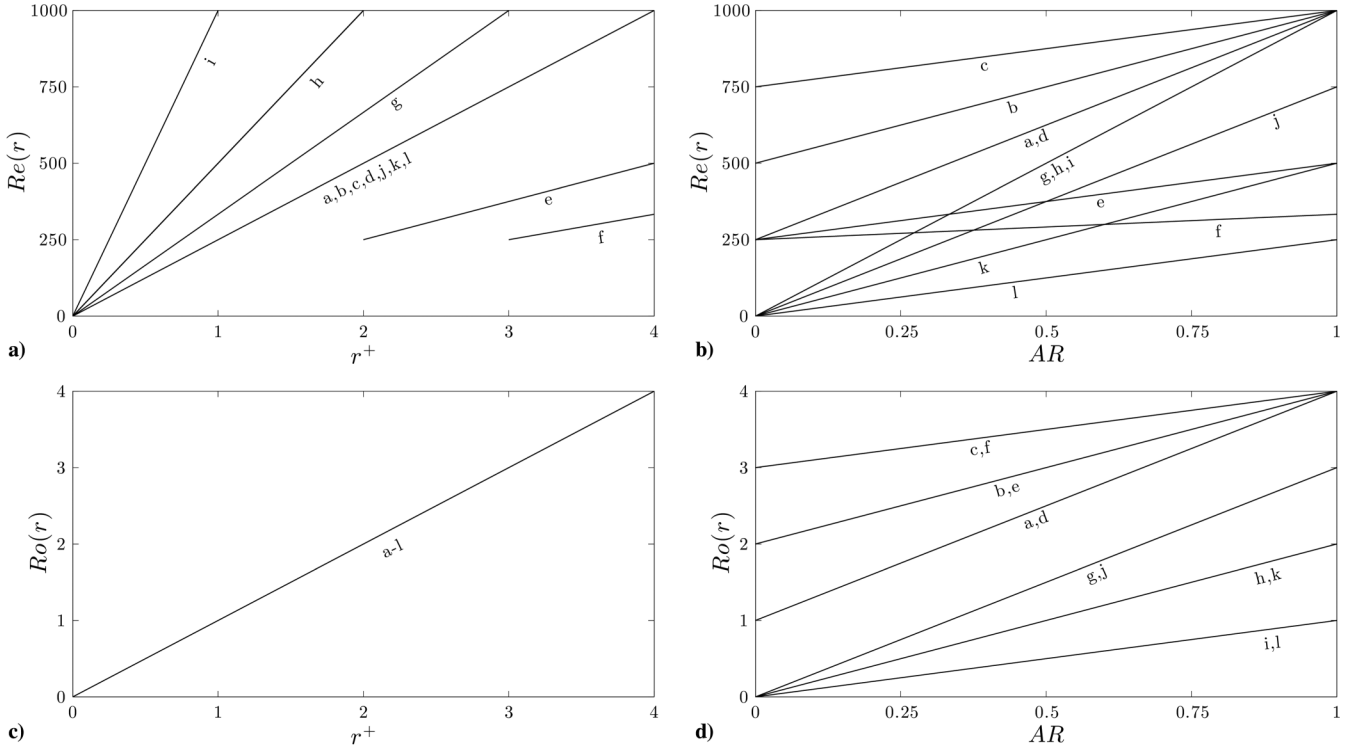

Fig. A3 Distributions in local Reynolds number $Re(r)$ (Figs. A3a and A3b) and Rossby $\mathrm{Ro}(r)$ number (Figs. A3c and A3d) as a function of r^+ (Figs. A3a and A3c) and R (Figs. A3b and A3d) for cases shown in Figs. 8 and A2.

References

[1] Wood, R. J., "The First Takeoff of a Biologically Inspired At-Scale Robotic Insect," *IEEE Transactions on Robotics*, Vol. 24, No. 2, 2008, pp. 341–347. doi:10.1109/TRO.2008.916997

[2] Jacobs, E. N., and Sherman, A., "Airfoil Section Characteristics as Affected by Variations of the Reynolds Number," NACA TR 586, 1939, pp. 227–267.

[3] Ringuette, M. J., Milano, M., and Gharib, M., "Role of the Tip Vortex in the Force Generation of Low-Aspect-Ratio Normal Flat Plates," *Journal of Fluid Mechanics*, Vol. 581, June 2007, pp. 453–468. doi:10.1017/S0022112007005976

[4] Jardin, T., Farcy, A., and David, L., "Three-Dimensional Effects in Hovering Flapping Flight," *Journal of Fluid Mechanics*, Vol. 702, July 2012, pp. 102–125. doi:10.1017/jfm.2012.163

[5] Taira, K., and Colonius, T. I. M., "Three-Dimensional Flows Around Low-Aspect-Ratio Flat-Plate Wings at Low Reynolds Numbers," *Journal of Fluid Mechanics*, Vol. 623, March 2009, pp. 187–207. doi:10.1017/S0022112008005314

[6] Kruyt, J. W., van Heijst, G. F., Altshuler, D. L., and Lentink, D., "Power Reduction and the Radial Limit of Stall Delay in Revolving Wings of Different Aspect Ratio," *Journal of The Royal Society Interface*, Vol. 12, No. 105, 2015, Paper 20150051. doi:10.1098/rsif.2015.0051

[7] Ellington, C. P., Van Den Berg, C., Willmott, A. P., and Thomas, A. L., "Leading-Edge Vortices in Insect Flight," *Nature*, Vol. 384, No. 6610, 1996, pp. 626–630. doi:10.1038/384626a0

[8] Dickinson, M. H., Lehmann, F. O., and Sane, S. P., "Wing Rotation and the Aerodynamic Basis of Insect Flight," *Science*, Vol. 284, No. 5422, 1999, pp. 1954–1960. doi:10.1126/science.284.5422.1954

[9] Lentink, D., Dickson, W. B., Van Leeuwen, J. L., and Dickinson, M. H., "Leading-Edge Vortices Elevate Lift of Autorotating Plant Seeds," *Science*, Vol. 324, No. 5933, 2009, pp. 1438–1440. doi:10.1126/science.1174196

[10] Lentink, D., and Dickinson, M. H., "Rotational Accelerations Stabilize Leading Edge Vortices on Revolving Fly Wings," *Journal of Experimental Biology*, Vol. 212, No. 16, 2009, pp. 2705–2719. doi:10.1242/jeb.022269

[11] Beem, H. R., Rival, D. E., and Triantafyllou, M. S., "On the Stabilization of Leading-Edge Vortices with Spanwise Flow," *Experiments in Fluids*, Vol. 52, No. 2, 2012, pp. 511–517. doi:10.1007/s00348-011-1241-9

[12] Garmann, D. J., and Visbal, M. R., "Dynamics of Revolving Wings for Various Aspect Ratios," *Journal of Fluid Mechanics*, Vol. 748, June 2014, pp. 932–956. doi:10.1017/jfm.2014.212

[13] Jardin, T., and David, L., "Spanwise Gradients in Flow Speed Help Stabilize Leading-Edge Vortices on Revolving Wings," *Physical Review E*, Vol. 90, No. 1, 2014, Paper 013011. doi:10.1103/PhysRevE.90.013011

[14] Jardin, T., and David, L., "Coriolis Effects Enhance Lift on Revolving Wings," *Physical Review E*, Vol. 91, No. 3, 2015, Paper 031001. doi:10.1103/PhysRevE.91.031001

[15] Wolfinger, M., and Rockwell, D., "Flow Structure on a Rotating Wing: Effect of Radius of Gyration," *Journal of Fluid Mechanics*, Vol. 755, Sept. 2014, pp. 83–110. doi:10.1017/jfm.2014.383

[16] Carr, Z. R., DeVoria, A. C., and Ringuette, M. J., "Aspect-Ratio Effects on Rotating Wings: Circulation and Forces," *Journal of Fluid Mechanics*, Vol. 767, March 2015, pp. 497–525. doi:10.1017/jfm.2015.44

[17] Schlueter, K. L., Jones, A. R., Granlund, K., and Ol, M., "Effect of Root Cutout on Force Coefficients of Rotating Wings," *AIAA Journal*, Vol. 52, No. 6, 2014, pp. 1322–1325. doi:10.2514/1.J052821

[18] Garmann, D. J., Visbal, M. R., and Orkwis, P. D., "Three-Dimensional Flow Structure and Aerodynamic Loading on a Revolving Wing," *Physics of Fluids*, Vol. 25, No. 3, 2013, Paper 034101. doi:10.1063/1.4794753

[19] Bury, Y., and Jardin, T., "Transitions to Chaos in the Wake of an Axisymmetric Bluff Body," *Physics Letters A*, Vol. 376, No. 45, 2012, pp. 3219–3222. doi:10.1016/j.physleta.2012.09.011

[20] Ozen, C. A., and Rockwell, D., "Flow Structure on a Rotating Plate," *Experiments in Fluids*, Vol. 52, No. 1, 2012, pp. 207–223. doi:10.1007/s00348-011-1215-y

[21] Ozen, C. A., and Rockwell, D., "Three-Dimensional Vortex Structure on a Rotating Wing," *Journal of Fluid Mechanics*, Vol. 707, Sept. 2012, pp. 541–550. doi:10.1017/jfm.2012.298

[22] Carr, Z. R., Chen, C., and Ringuette, M. J., "Finite-Span Rotating Wings: Three-Dimensional Vortex Formation and Variations with Aspect Ratio," *Experiments in Fluids*, Vol. 54, No. 2, 2013, pp. 1–26. doi:10.1007/s00348-012-1444-8

[23] Medina, A., and Jones, A. R., "Stereoscopic PIV Analysis on Rotary Plates in Bursting," *33rd AIAA Applied Aerodynamics Conference*, AIAA Paper 2015-3297, 2015.

[24] Percin, M., and van Oudheusden, B., "Three-Dimensional Flow Structures and Unsteady Forces on Pitching and Surging Revolving Flat Plates," *Experiments in Fluids*, Vol. 56, No. 1, 2015, pp. 1–19. doi:10.1007/s00348-014-1876-4

[25] Jones, A. R., Medina, A., Spooner, H., and Mulleners, K., "Characterizing a Burst Leading-Edge Vortex on a Rotating Flat Plate Wing," *Experiments in Fluids*, Vol. 57, No. 4, 2016, pp. 1–16. doi:10.1007/s00348-016-2143-7

[26] Huang, Y., Venning, J., Thompson, M. C., and Sheridan, J., "Vortex Separation and Interaction in the Wake of Inclined Trapezoidal Plates," *Journal of Fluid Mechanics*, Vol. 771, May 2015, pp. 341–369. doi:10.1017/jfm.2015.160

M. Green
Associate Editor